Article

Operando X-ray imaging reveals size-dependent evolution of cobalt oxide thermochemical material during thermal redox cycles

Yuxiang Peng [1], Lyu Zhou[2], Madeline Van Winkle[3], Cheng-Chu Chung[1], Youyang Zhao[4], John Mangum[3], Xianghui Xiao [5], Katherine Jungjohann[3], Judith Vidal[6], Shuang Cui[2,6], Mingyuan Ge [5] & Yu-chen Karen Chen-Wiegart [1,5] ✉

Multivalent metal oxides are promising thermochemical materials (TCMs) for energy storage and conversion owing to their high energy density, air compatibility, and high-temperature stability. Co_3O_4 serves as a model system for examining particle-size- and structure-dependent redox behavior. While particle size and porosity are known to affect performance, their interplay and the kinetics of pore formation during cycling remain unclear. Here we show the chemical and 3D morphological evolution of Co_3O_4 micro- and nanoparticles during redox cycles at 800–900 °C using thermal analysis, in-situ synchrotron transmission X-ray microscopy (TXM), and scanning electron microscopy. Thermal analysis shows that nanoparticles re-oxidize more rapidly than microparticles at 800 °C. In-situ nanotomography and chemical imaging reveals that nanoparticles undergo redox conversion without forming internal pores, whereas microparticles develop isolated porosity during reduction. These pores persist through re-oxidation, correlating to a lower conversion rate in subsequent cycles. Our results demonstrate distinct degradation kinetics in Co_3O_4 micro- and nanoparticles, underscoring the critical role of particle size and porosity in redox performance and informing strategies to enhance the long-term efficiency of metal oxide TCMs.

As the global energy landscape shifts towards sustainable sources, the need for efficient and durable thermal energy storage (TES) materials is becoming increasingly critical in many applications, such as concentrated solar power systems[1,2]. Among TES materials, thermochemical materials (TCMs) have gained significant attention in recent years due to their competitive energy density and capability to operate at higher temperatures[3,4]. Multivalent metal oxides undergoing redox reactions, typically in an open system at temperatures above 700 °C, are promising TCMs because they can operate with air as the working fluid[5,6].

[1]Department of Materials Science and Chemical Engineering, Stony Brook University, Stony Brook, NY, USA. [2]Department of Mechanical Engineering, The University of Texas at Dallas, Richardson, TX, USA. [3]Materials Science Center, National Renewable Energy Laboratory, Golden, CO, USA. [4]Center for Energy Conversion and Storage Systems, National Renewable Energy Laboratory, Golden, CO, USA. [5]National Synchrotron Light Source II (NSLS-II), Brookhaven National Laboratory, Upton, NY, USA. [6]Buildings Technologies and Science Center, National Renewable Energy Laboratory, Golden, CO, USA. ✉e-mail: Karen.Chen-Wiegart@stonybrook.edu

Multivalent metal oxides have emerged as promising TCMs for TES systems because of their high energy storage capacity, favorable reaction reversibility, suitable redox temperatures, and cost-effective working atmosphere[7–10]. However, challenges such as limited material reversibility and performance degradation over multiple cycles remain[11–13]. Among these oxides, Co_3O_4 is an ideal candidate for mechanistic studies, despite its relatively high material cost. Its well-characterized redox behavior[14] enables clear evaluation of reaction kinetics and pathways at the nano- and meso-scales, providing insights that can guide the development of more cost-effective TCMs. One of the degradation issues is structural deformation, such as cracking and fragmentation, induced by thermal cycling, likely resulting from repeated thermal expansion and contraction[15,16]. Another common degradation mechanism in Co_3O_4 is the sintering of particles at elevated temperatures, which impedes diffusion of gaseous species and leads to reduced storage capacity[11,12]. Common mitigation strategies, such as reducing the initial particle size[7,17,18] or introducing a porous structure[7,16,19], have been applied to Co_3O_4 and doped Co_3O_4 TCMs to enhance their performance. While a porous structure is generally believed to improve redox rate by increasing surface area and facilitating gas transport, recent studies suggest that its benefits may not always be straightforward. For instance, a Co_3O_4–based porous, foam-like structure with a pore size of 1–1.5 mm exhibited a lower conversion rate during thermal cycling compared to a dense structure; furthermore, the porosity of both dense and porous Co_3O_4 changed after 10 thermal redox cycles[15]. These findings highlight that, beyond simply introducing porosity, it is critical to ensure the stability of the porous structure throughout thermal cycling. Recent studies suggest that preserving the porous structure in TCMs through lattice-matching strategies and the addition of stabilizers can help maintain effective thermal cycling performance[20,21]. Similarly, nanoparticles are generally believed to improve Co_3O_4 conversion rate by increasing reactive surface area and reducing diffusion distances[7,11]. Therefore, it is important to track the evolution of the porous structure within particles with different sizes during thermal cycling to better understand their conversion efficiency. However, the kinetics of the pore evolution, both within and between individual particles, especially the isolated pores, remain poorly understood. Traditional technique, like the Brunauer-Emmett-Teller (BET) method based on adsorption isotherms of nonreactive nitrogen or argon[22], commonly used for porosity measurements, has limitations in analyzing internal and isolated pores at the sub-particle level. As a result, the influence of particle size and isolated pores on the chemical and morphological evolution of Co_3O_4 during thermal cycling has not been thoroughly explored, partly due to the challenges in characterizing intermediate morphological and oxidation state changes at the micron and nanometer scales in situ during the thermal cycling.

Synchrotron transmission X-ray microscopy (TXM) has been employed in various studies to characterize the morphological evolution of materials. For instance, in battery research[23,24], it allows for direct 3D imaging of a range of materials under real-time cycling conditions. Additionally, changes in material interfaces, such as coarsening[25] and alterations in the pore/ligament network[26] over time, can be captured and quantified. Moreover, the spatial distribution of chemical information and oxidation states in materials can be directly visualized and quantified using X-ray absorption near-edge structure (XANES) imaging, a spectroscopic imaging technique[27,28]. These time-resolved synchrotron-based techniques can capture the morphological evolution and spatially resolved chemical changes of Co_3O_4 during thermal cycles at sub-30 nm resolution, providing insights into how morphological changes under high-temperature thermal cycling affect the thermal redox reaction.

In this work, Co_3O_4 micro- and nano-particles were selected to study their chemical and morphological evolution, as well as their reversibility dur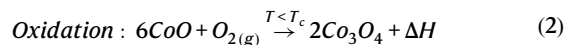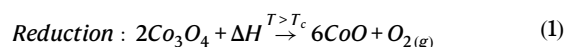ing thermal redox cycles. Since the transition temperature of Co_3O_4 to CoO was reported to be 885 °C[13], the temperature range for the thermal redox cycle in this study was set between 800 and 900 °C. At the macro-scale, thermal analysis was performed on these two materials using thermogravimetric analysis (TGA). At the micron to tens of nm length scale, the morphological and chemical evolution of the materials in an air atmosphere during thermal redox cycles was studied using in-situ TXM and 2D XANES imaging techniques. For further analysis, the in-situ samples after thermal redox cycles were analyzed using scanning electron microscopy (SEM). Through the investigation and analysis of the morphological evolution and chemical changes of Co_3O_4 in different particle sizes at various scales, the fundamental phase transition and degradation mechanisms of Co_3O_4 TCM during thermal redox cycles in air are discussed.

Results and discussion
TGA results
To investigate the reversibility and kinetics of the conversion between Co_3O_4 and CoO, the redox behaviors of Co_3O_4 micro and nano particles were analyzed by TGA in one and five thermal redox cycles between 800 °C and 900 °C. The results are shown in Fig. 1.

As shown in Fig. 1A, B, both the micro and nano particles of Co_3O_4 rapidly converted to CoO at 900 °C during the first cycle, as indicated by the significant weight loss accompanied by O_2 evolution. The theoretical calculation shows that the expected weight loss in the full conversion of Co_3O_4 to CoO is 6.6 wt%, following the reaction shown in Eqs. (1, 2).

$$Reduction: 2Co_3O_4 + \Delta H \xrightarrow{T > T_c} 6CoO + O_{2(g)} \quad (1)$$

$$Oxidation: 6CoO + O_{2(g)} \xrightarrow{T < T_c} 2Co_3O_4 + \Delta H \quad (2)$$

Where T is temperature and T_c is transition temperature. The normalized weight was calculated as the ratio between the difference of the theoretical and actual weight losses to theoretical weight loss, and the experimental results are presented in Fig. S1. During the cooling process, the reverse direction of the reaction (2) took place. Initially, there was no significant weight change for the particles at 850 °C. To further investigate the temperature of the re-oxidation reaction, additional TGA scans were conducted under a controlled cooling rate of 2 °C/min, and the result is shown in Fig. S2. But at 800 °C, the nanoparticles increased in weight rapidly and fully converted to Co_3O_4 in approximately 5 min. In contrast, the microparticles increased in weight at a slower rate, and did not fully convert even after 30 min. To further examine the conversion fraction of CoO during the reoxidation process, we performed additional simultaneous TGA–DSC experiments, with the results presented in Fig. S3. As shown in Fig. 1C, D, there was no significant difference in the weight change for the Co_3O_4 particles over five cycles. Additionally, the derivative of mass change remained consistent across the five cycles for both the micro- and nanoparticles, indicating that the conversion rate of Co_3O_4 did not change and that both particle types retained their reversibility throughout the cycles. Therefore, there was no obvious degradation in the micro and nano particles of Co_3O_4 during the short-term thermal redox cycles under the current cycling conditions, which is consistent with the literature data[19].

Chemical evolution analyzed by in-situ 2D XANES imaging
To study the chemical evolution and kinetic differences between Co_3O_4 microparticles and nanoparticles during thermal redox cycles, 2D XANES images were collected at various time points in the temperature range of 800 to 900 °C at the FXI beamline. Fig. 2, Supplementary Movie 1 and Supplementary Movie 2 show the fitted 2D XANES images of Co_3O_4 microparticles and nanoparticles, with each pixel corresponding to the atomic fraction of Co in the CoO phase,
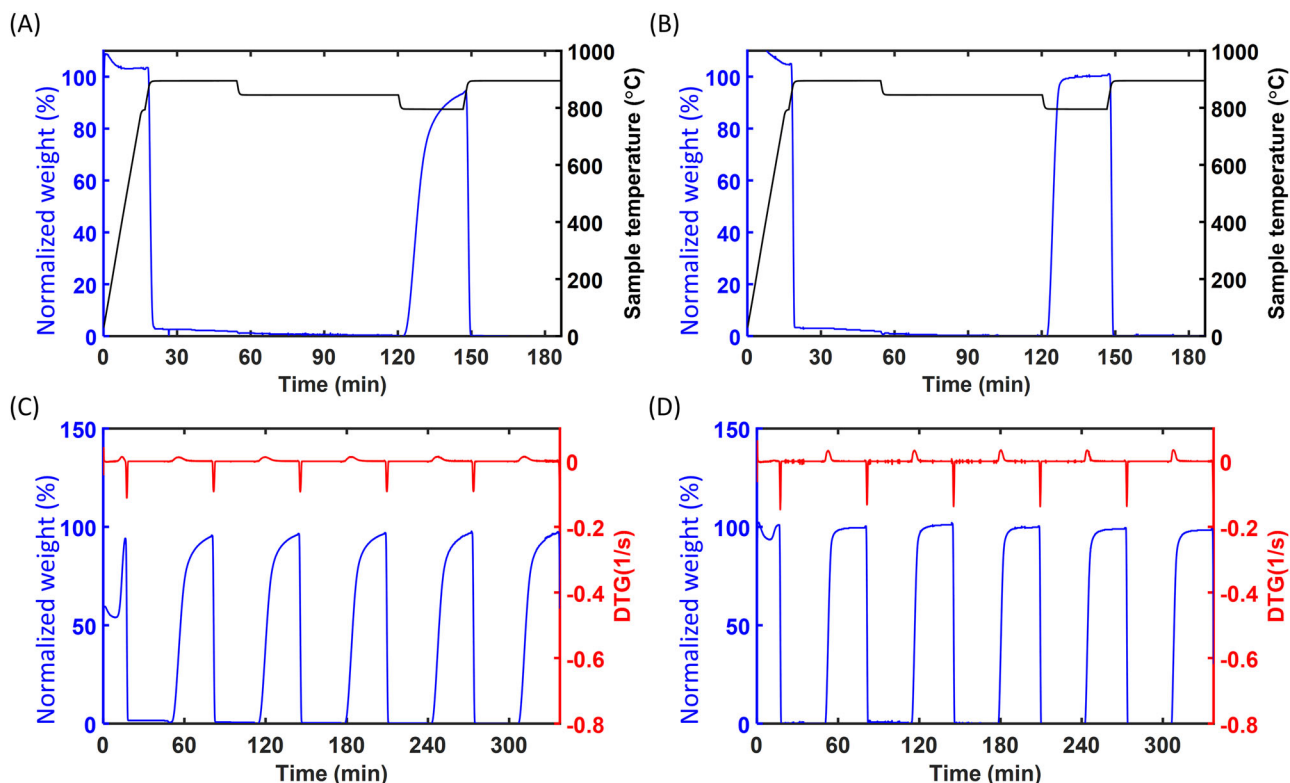
Fig. 1 | Thermogravimetric analysis curves of Co₃O₄ microparticles and nanoparticles during one and five thermal redox cycles; blue lines represent normalized weight (the difference between theoretical and actual weight loss, divided by theoretical weight loss, for a complete Co₃O₄-to-CoO conversion), black lines indicate the temperature profile, and red lines show the derivative of mass change (DTG). (**A**, **B**) normalized weight of microparticles (**A**) and nanoparticles (**B**) during one redox cycle (900–850–800–900 °C); (**C**, **D**) normalized weight and DTG curves of microparticles (**C**) and nanoparticles (**D**) over five redox cycles (900–800 °C) with 30 min holding time at each temperature. Source data are provided as a Source Data file.

based on the white line positions. This was determined by the linear combination fitting of normalized XANES spectra of CoO and Co₃O₄, and the fraction of CoO spectrum used in the fitting corresponds to the atomic fraction of Co in the CoO phase; for simplicity, the term "fraction of CoO" will be used for the remainder of the manuscript.

In Fig. 2A, a nearly full conversion of Co₃O₄ to CoO was observed in the microparticles during the first cycle at 900 °C within a short time (~3 min), which is consistent with the TGA results (Fig. 1). When the temperature cooled down to 850 °C, CoO gradually converted back to Co₃O₄ through reoxidation. Detailed XANES spectra at different locations, from the center region to the surface, are shown in Fig. S4. However, CoO did not fully convert back to Co₃O₄ after 55 min, indicating a kinetically limited reoxidation process. The incomplete reoxidation process and the resulting chemical heterogeneity can be visualized in Fig. 2B: the region of interests (ROIs) in the enlarged view of Fig. 2A–h, along with the corresponding spectra, identifies a mixture of the Co₃O₄ (purple) and residual CoO (yellow). Fig. 2C shows the temperature profile of the imaging data collection from Fig. 2Aa–p.

In the in-situ 2D XANES analysis, the conversion from CoO to Co₃O₄ occurred at ~850 °C, as shown in Fig. 2Ae–h, but this re-oxidation process did not initiate in the TGA analysis at this temperature. A separate DSC thermal analysis determined that the re-oxidation process of the microparticles initiate at ~850 °C, as shown in Fig. S5. Literature reports the onset re-oxidation temperature as 850 °C[12], 870 °C[13], and 879.7 °C[5]. These variations can reasonably be attributed to kinetic factors such as sample geometry, mass, and heat transfer behavior. Therefore, 850 °C is likely the equilibrium temperature during the re-oxidation process in the TXM experiment. If the experimental temperature is slightly below this equilibrium temperature, it may promote the conversion to Co₃O₄, whereas if it is slightly above, the conversion may be inhibited.

Since the reoxidation process was incomplete, the temperature was further decreased to 800 °C, with results shown in Fig. 2Ai–l. At 800 °C, most CoO converted back to Co₃O₄ within a short period of time (~3 min), but a small amount of the CoO did not convert back to Co₃O₄ after 21 min. In the subsequent cycle, when the temperature was increased back to 900 °C, the conversion rate of Co₃O₄ to CoO was significantly decreased compared to the first cycle at 900 °C. It can be seen in Fig. 2Am–p that the reduction process took longer in the second cycle, with a small amount of Co₃O₄ not converting to CoO after 30 min.

To study the Co₃O₄ nanoparticles, 2D XANES imaging with a similar temperature profile (Fig. 2F) as microparticles was conducted at the FXI beamline, with the results shown in Fig. 2D, E. As shown in Fig. 2D, the Co₃O₄ nanoparticles rapidly converted to CoO within the first 3 min during the first cycle at 900 °C. However, upon cooling, the CoO phase did not fully convert back to Co₃O₄ within 30 min at 850 °C, leaving a small amount of the nanoparticles unreacted. The normalized XANES spectra extracted from the selected ROIs from images, as shown in Fig. 2E, indicate that some CoO phase remained in the particles, particularly in ROI-2. When the temperature was further lowered to 800 °C, most of the CoO converted to Co₃O₄ within ~3 min. Notably, in the second cycle at 900 °C, the conversion rate of Co₃O₄ nanoparticles was faster than that of the microparticles, with most of Co₃O₄ converting to CoO within ~3 min, which was in the same conversion rate as the first cycle. Since the specific surface area (surface area per volume) of nanoparticles is larger than microparticles, there is a larger amount of the interfaces between air and nanoparticles where the oxidation process can take place. Consequently, the rate of the re-oxidation process was faster in the nanoparticles, leading to a faster conversion rate between Co₃O₄ and CoO during the thermal redox cycles.
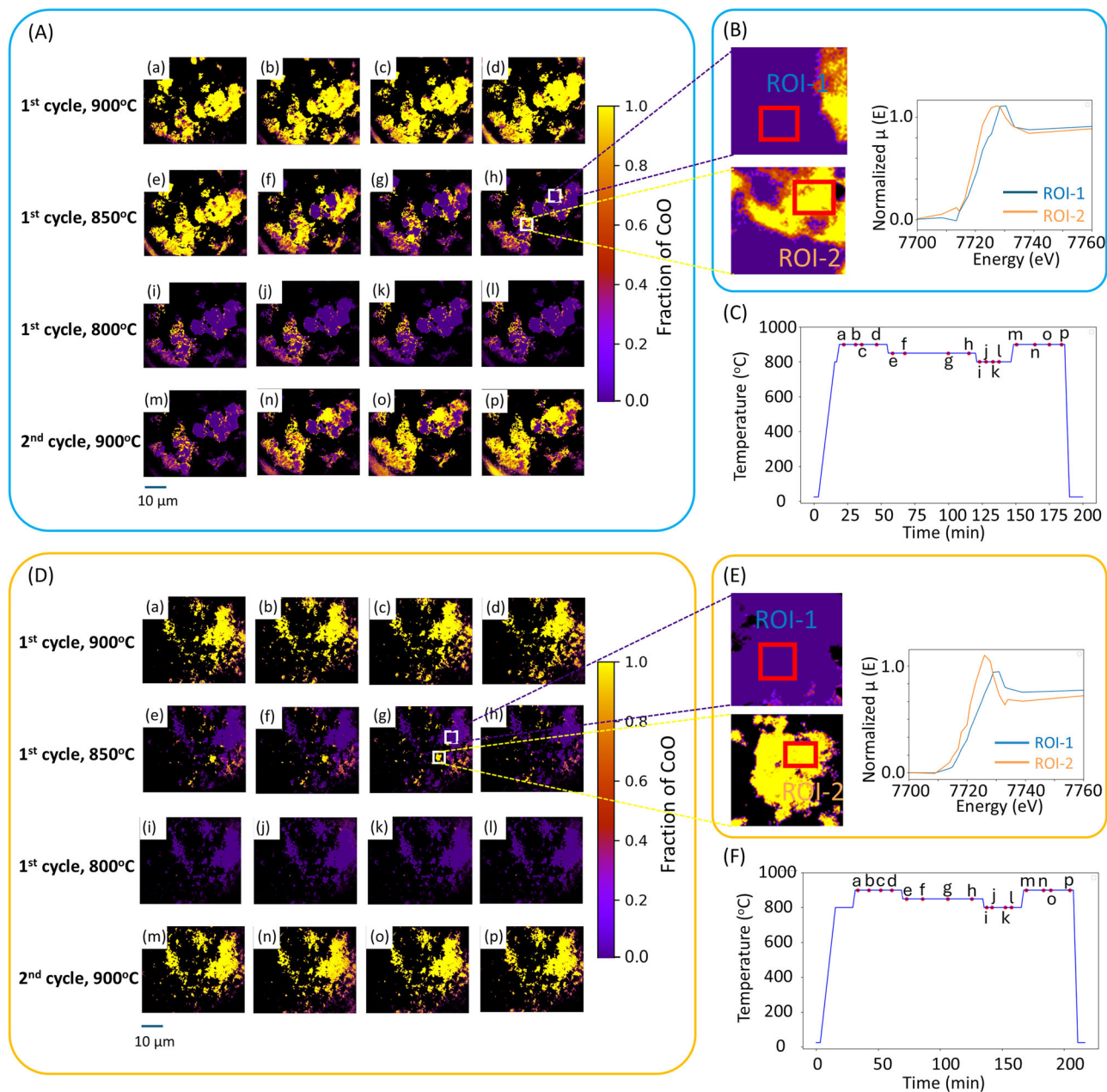
Fig. 2 | The evolution of chemical states of Co_3O_4 for different particle sizes as a function of thermal redox cycles. (**A**–**C**) microparticles and (**D**–**F**) nanoparticles: (**A**, **D**) Fitted 2D XANES images reflecting the atomic ratio of Co in CoO phase at different temperatures and time points. (**B**, **E**) Enlarged view of (**A**–**h**) for microparticles and (**D**–**g**) for nanoparticles, highlighting particle heterogeneity in the region of interest (ROI) and corresponding XANES spectra, where μ indicates the X-ray attenuation. (**C**, **F**) Temperature profile during the in-situ experiment, indicating time points (a-p) for imaging data collection. Note that black color in the XANES images indicates a masked region where the sample amount is negligible. Source data are provided as a Source Data file.

To quantify the conversion rate of the Co_3O_4 micro- and nanoparticles, the amount of Co (arbitrary unit, proportional to the mol. of Co) in each pixel of the 2D XANES images was calculated. The fraction of CoO in the total sample and the conversion depending on the amount of Co, during the thermal redox cycles, are shown in Fig. 3, for both the micro- and nano-particles.

Figure 3A shows that the conversion rate of Co_3O_4 microparticles to CoO at 900 °C is faster in the first cycle (reaching > 95.0% in ~25 min after the temperature reaching 900 °C) than in the second cycle (reaching only ~60.0% in ~25 min). In contrast, ~95.0% of Co_3O_4 nanoparticles converted to CoO within 2 min at 900 °C in both the first and second cycles, as shown in Fig. 3B. The conversion rate significantly decreased for microparticles during the second cycle but remained

unchanged for nanoparticles, possibly due to morphological changes in the microparticles during the first thermal cycle.

In Fig. 3C, microparticles in regions with higher Co amount (thicker regions) converted to Co_3O_4 to a greater extent (in fraction) than those with less Co amount (thinner regions) at 850 °C and 800 °C. This might be because the specific surface area and surface curvature increase significantly in the thicker regions at 900 °C, promoting conversion to Co_3O_4 when the temperature is lowered. The larger specific surface area may be due to the thicker region being composed of a large number of small particles. As shown in Fig. 3D, the thicker and thinner regions of the nanoparticle sample exhibited similar conversion rates when the temperature was lowered to 850 °C and 800 °C, suggesting that this morphological evolution did not occur in
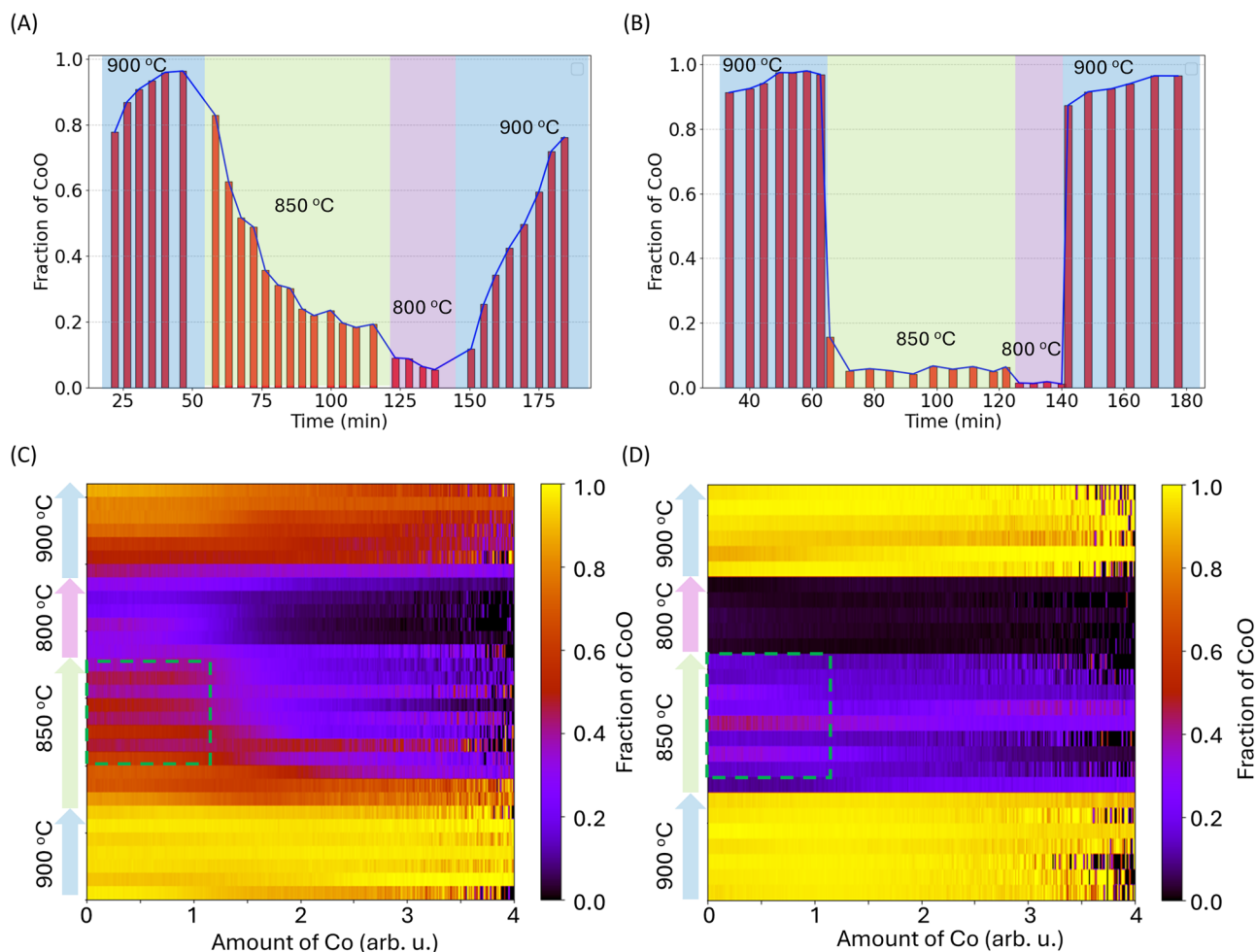
Fig. 3 | Fraction of CoO and Co-amount-dependent redox conversion in microparticles and nanoparticles during thermal cycling. The fraction of CoO in the microparticle (**A**) and nanoparticle (**B**), during thermal redox cycles. The shaded background colors represent different temperature segments applied during the cycles. **C**, **D** show the conversion as a function of the amount of Co per pixel, given in relative units proportional to the molar amount of Co, in the microparticle and nanoparticle, respectively, which are calculated based on the 2D XANES images. The green dashed rectangles highlight the back-and-forth conversion between Co_3O_4 and CoO at 850 °C.

nanoparticles at 900 °C. To better understand the differences in redox behavior between micro- and nanoparticles, the morphological changes during thermal redox cycles will be discussed in the following section. Interestingly, both micro- and nanoparticles converted to CoO back and forth at 850 °C (green-color dash rectangles in Fig. 3C, D), indicating that 850 °C is the equilibrium temperature for the re-oxidation process.

Morphological evolution analyzed by in-situ X-ray nano-tomography

To understand the morphological evolution with time of Co_3O_4 micro and nano particles, the in-situ X-ray nano-tomography data were collected at the end point of each temperature segment. The 3D volume rendering, as well as the corresponding 2D XY and XZ pseudo cross-sectional views of Co_3O_4 micro and nano particles during the thermal redox cycles at different temperatures, are shown in Fig. 4.

In microparticles, as shown in Fig. 4A–C, several large particles were observed in the first cycle at 800 °C before any chemical evolution, and no porosities were present inside the particles. However, after ramping the temperature to 900 °C, cooling to 850 °C, and then down to 800 °C, porous structures appeared within the particles, as shown in the detailed 2D XY and XZ views shown in Fig. 4A, B. Figure 4C shows the 3D volume rendering of the particles, with the internal and isolated pores displayed in the sub-figures. Internal pores formed within a

particle because of O_2 evolution, whereas isolated pores originated from sintering. At 850 °C, the volume of internal and isolated pores (shown in magenta) increased significantly within the particles during the back-and-forth conversion between Co_3O_4 and CoO. This conversion process likely promoted sintering, causing the particles to connect and form large isolated pores. The volume fraction of internal and isolated pores (calculated as the volume of internal pores divided by the volume of particles and internal and isolated pores) was 8.2% at 850 °C, decreasing to 7.2% at 800 °C due to more CoO being converted. These internal and isolated pores likely inhibited the reduction of Co_3O_4 to CoO during the second cycle at 900 °C. However, this back-and-forth conversion was not observed in the TGA results, suggesting that fewer internal and isolated pores were generated within the particles. Thus, the subsequent reduction process remained as fast as in the first cycle. A detailed discussion of internal and open pores is provided in section 2.4. These porous structures persisted in the particles even after completing the thermal redox cycles and returning to room temperature. In contrast, these porous structures were not observed in the nanoparticles during the thermal cycles, as shown in Fig. 4D–F. The nanoparticles retained their original morphology without agglomeration or merging after the thermal redox cycles. To further understand the morphological evolution of the microparticles and nanoparticles during the thermal cycles, the surface area and volume changes for these two samples as a function of the thermal cycling are shown in Fig. S6.
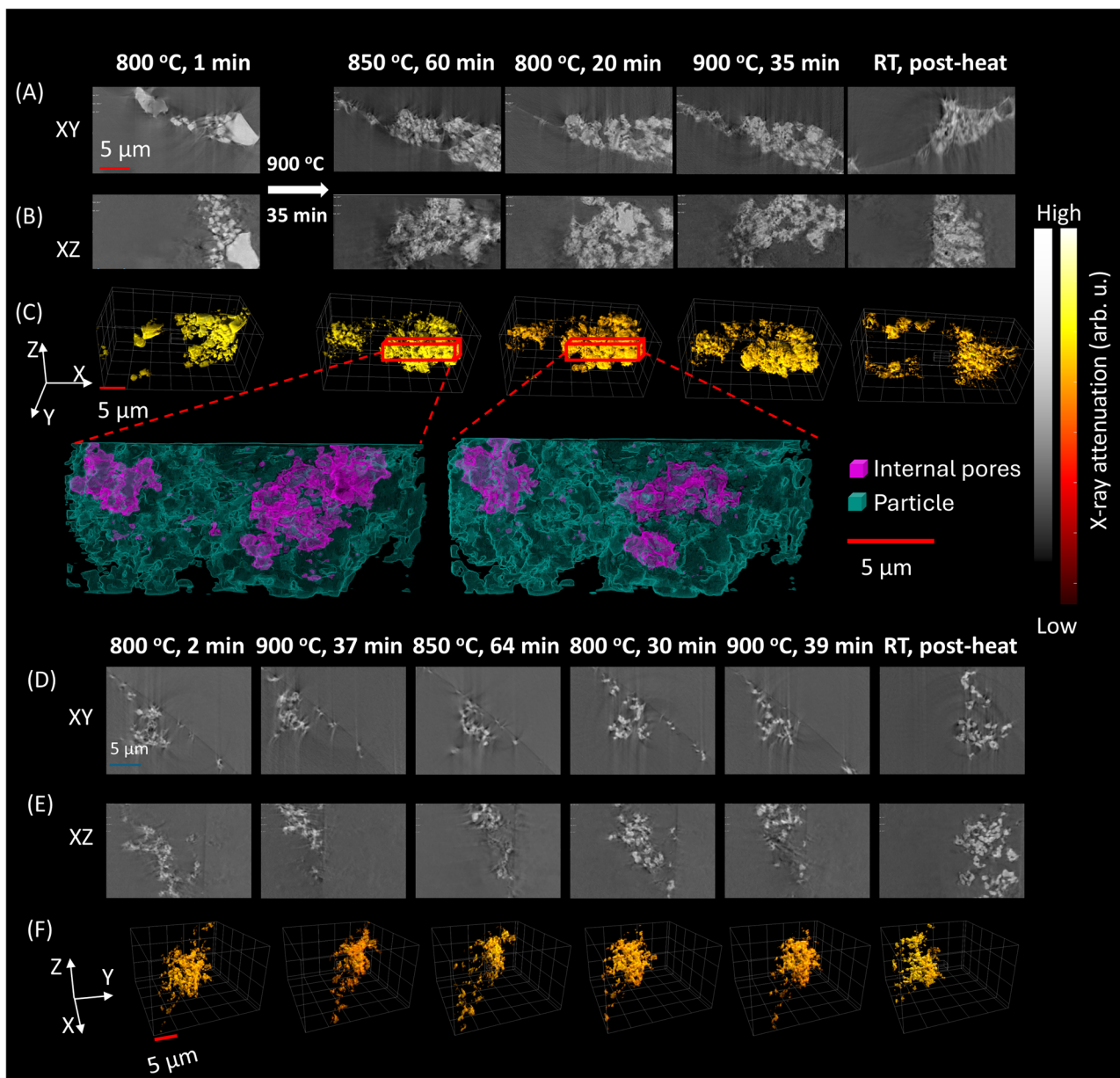
Fig. 4 | 3D morphological evolution of Co$_3$O$_4$ microparticles and nanoparticles in air during thermal redox cycles between 800 °C, 850 °C and 900 °C, characterized by in-situ synchrotron X-ray nano-tomography at different time points. 2D (XY and XZ) pseudo-cross-sectional views of microparticles (**A**, **B**) and nanoparticles (**D**, **E**). 3D volume rendering of microparticles (**C**) with sub-figures showing the internal and isolated pores and nanoparticles (**F**).

Based on the chemical evolution kinetics shown in Figs. 2, 3, the formation of a porous structure in the microparticles may have hindered the conversion from Co$_3$O$_4$ to CoO during the second cycle at 900 °C, as the slower conversion rate was not observed in nanoparticles. While porosity can increase the surface area and potentially enhance the interaction between cobalt oxide and oxygen, the internal and isolated pores likely contribute, affecting the overall conversion process. The porosity evolution will be further explored in the following sections.

Porosity evolution and impact on Co$_3$O$_4$/CoO conversion during thermal redox cycles

To fully understand the mechanism behind the formation of the porous structure inside the Co$_3$O$_4$ microparticles, another in-situ X-ray nano-tomography experiment of Co$_3$O$_4$ microparticles during thermal redox cycles between 800 °C and 900 °C was conducted at the FXI beamline. A single Co$_3$O$_4$ microparticle was continuously measured

with X-ray nano-tomography throughout the thermal redox cycles, and the morphological evolution of the particle and porous structure visualized in 3D are shown in Fig. 5, Supplementary Movie 3 at different temperatures and time points.

A smooth surface was observed on the particle at room temperature, as shown in Fig. 5Aa, but it became rougher when the temperature was raised to 900 °C, shown in Fig. 5Ac, d. This surface character did not change significantly during the following thermal redox cycle (Fig. 5Ae–h). Since both the surface area and volume of the single particle changed due to the O$_2$ evolution, here, the specific surface area (SSA) was calculated by dividing the surface area (including from both internal and open pores) by volume to characterize the surface and porosity properties of the particle. The plot of SSA versus time is shown in Fig. 5B, overlaid with the temperature profile during the thermal cycling. The specific surface area increased significantly at the beginning of the first cycle at 900 °C, indicating that smaller pores were generated inside the particle with O$_2$ evolution. O$_2$
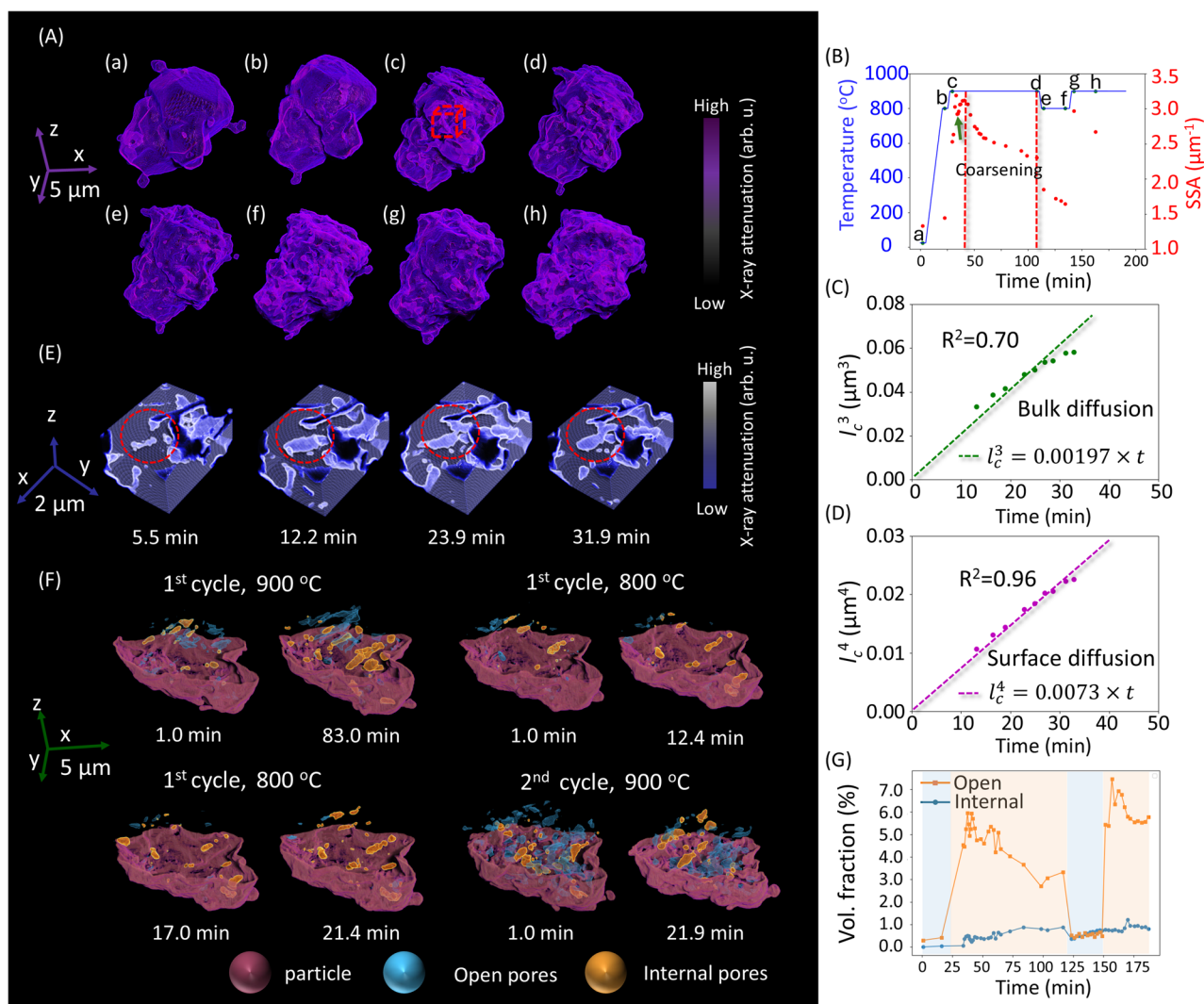
Fig. 5 | Morphological evolution, coarsening mechanism, and formation of a porous structure, visualized and quantified from a single Co_3O_4 microparticle during thermal redox cycles between 800 and 900 °C. (**A**) Morphological evolution of Co_3O_4 microparticle at different temperature points as shown in the temperature heating profile in (**B**). **B** Temperature profile during the in-situ X-ray nano-tomography experiment, indicating the time points of tomography scans from image data (a) to (h), along with the plot of specific surface area (SSA) vs. time. **C**, **D** Power-law fitting of characteristic length (l_c) vs. time for bulk-diffusion and surface-diffusion coarsening mechanism. **E** Enlarged 3D view of morphological evolution in red cubic region as shown in sub-figure (**A**-c) during the coarsening process in the 1st cycle at 900 °C. **F** Formation of internal and open pores within the particle over the isothermal heating time at different temperatures. **G** Plot of the volume of open and internal pores within the particle during thermal redox cycles (initial time starting from room temperature, light blue region at 800 °C and light orange region at 900 °C). Note that the time points marked in (**A**), (**E**), and (**F**) are relative to the beginning of each temperature heating segment. Source data are provided as a Source Data file.

evolution could lead to a sudden generation of a large amount of vacancies, which then diffuse through the lattice, forming the initial small pores when there is excess concentration of vacancies[29].

Following the initial rapid generation of pores, there was then a sudden decrease in specific surface area at 900 °C observed at ~6 min (as indicated by the green arrow in Fig. 5B), which might be due to the coarsening process of the surface with high curvatures, corresponding to the small features such as pores generated from the O_2 evolution[30]. The continued evolving oxygen gas caused the pores to grow further, eventually slowing down and stopping after 12 min of heating the sample at 900 °C, as evidenced by the steady decrease in specific surface area. Coarsening became the dominant process after 12 min at 900 °C, with smaller pores merging into larger ones and larger pores interconnecting to form pore networks, which will be further discussed in Fig. 5E. The driving force for coarsening here is to reduce the total surface energy of the system by reducing the amount of the surface[31].

To further understand the kinetics of coarsening in the Co_3O_4 particle, the power-law relationship between the characteristic length (l_c), which is reciprocal of specific surface area and coarsening time (t) was determined to provide insights into the coarsening mechanism. The l_c for materials with complex morphology has been used to analyze the morphological evolution of materials[26,32]. The coarsening time is determined relatively from the time when the temperature reached 900 °C. The power (n) was determined by fitting the experimental data to the following Eq. (3)[26]:

$$l_c^n \sim t, \tag{3}$$

where different values of n correspond to different mechanisms: $n = 3$ for bulk diffusion, and $n = 4$ for surface diffusion[26,33,34]. Other coarsening mechanisms, such as viscous flow and evaporation/recondensation, were not considered in this study. The fitting line was set to intercept at the origin, as coarsening likely began when the
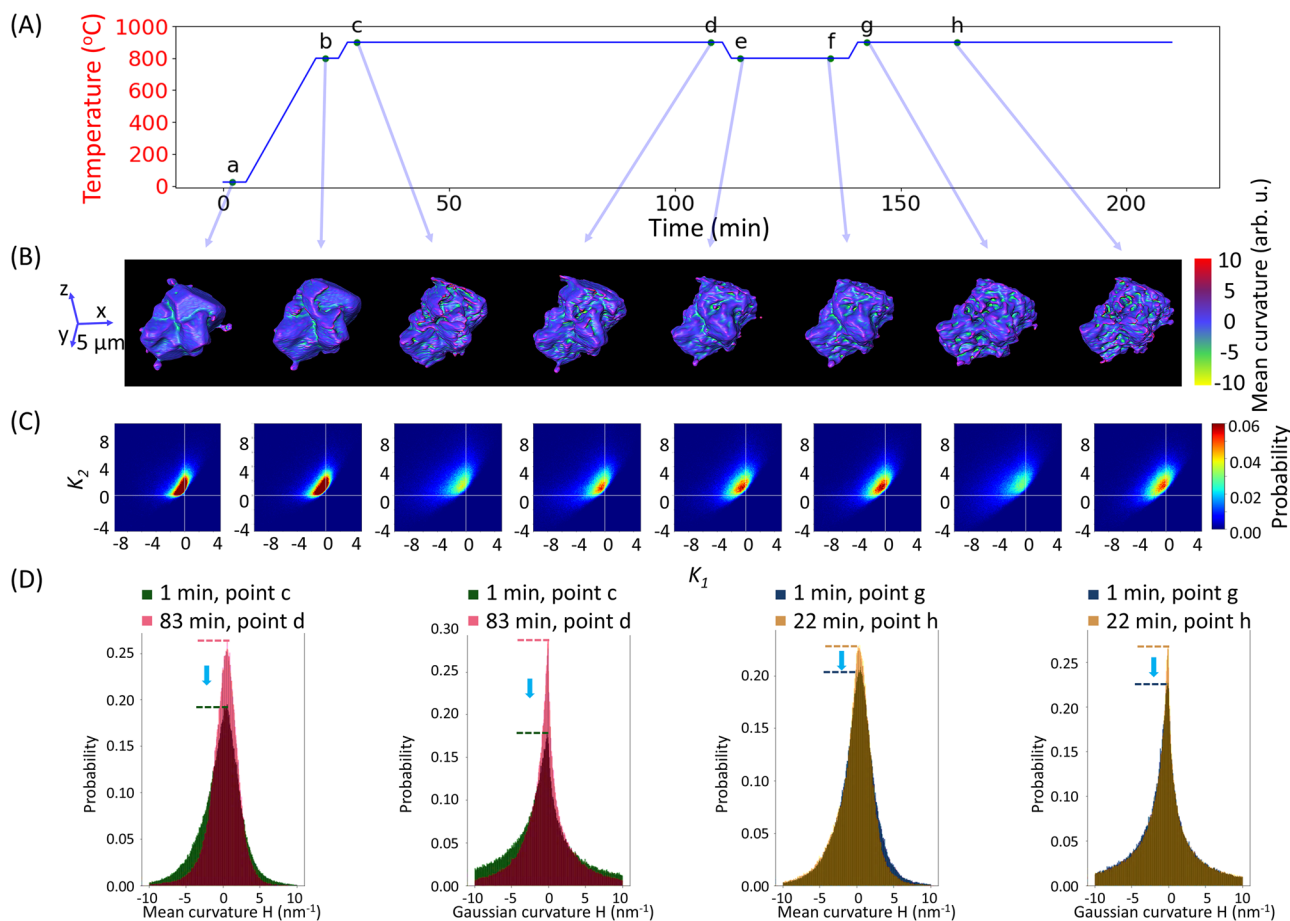
Fig. 6 | Quantitative curvature analysis of the Co₃O₄ particle during the thermal cycles. (**A**) Temperature profile during the in-situ X-ray nano-tomography experiment, with labeled data points (**a**–**h**) corresponding to the particle views in (**B**). **B** Surface rendering of the particle at different temperature points, as indicated in the temperature profile in (**A**). The surface is color-mapped by the local

mean curvature at each point. **C** Scaled interfacial shape distributions (K_1 vs. K_2) at different temperature points. **D** Histograms of the mean curvature ($H = (K_1 + K_2)/2$) and Gaussian curvature ($H = K_1 \cdot K_2$) at 900 °C during cycle 1, corresponding to points (**c**) and (**d**), and during cycle 2, corresponding to points (**g**) and (**h**).

temperature was raised to 900 °C. As shown in Fig. 5C, D; the fit of l_c^4 versus t exhibited a higher goodness-of-fit ($R^2 = 0.96$) than l_c^3 versus time ($R^2 = 0.70$). This result indicates that surface diffusion is the rate-determining mechanism controlling coarsening in the microparticles under this condition[33].

Figure 5E shows the morphology of pore formation inside the particle in a sub-region, as marked by a red dashed cube in Fig. 5Ac. In the region highlighted by a red circle, a small internal pore formed and continued to grow due to the evolution of O₂ gas, which could potentially increase the O₂ partial pressure within the pore. This early stage of morphological evolution was dominated by the kinetics of gas evolution and vacancy diffusion through the lattice (bulk diffusion) rather than surface diffusion coarsening. Following this initial small pore formation, to minimize surface energy, ions on the particle surface migrated from regions of high curvature, where there are sharp features and a higher chemical potential, to regions of lower curvature, where there are smoother features with a lower chemical potential. The curvature evolution will be further discussed in Fig. 6. As a result, the pore merged with another nearby pore through surface diffusion. Over time, the connected pores grew and the surface became smoother, ultimately forming a more stable microstructure.

Figure 5F, Supplementary Movie 4 show the evolution and changes of open and internal pores within the particle during the thermal cycles, and Fig. 5G illustrates the change in the volume of open pores and internal pores over time. During the O₂ evolution process in the first

cycle at 900 °C, both internal and open pores formed simultaneously. Open pores that opened to the air facilitated the evolution of O₂ during the conversion to CoO with an enlarged active surface area. Conversely, internal pores trapped O₂, increasing its local concentration and thermodynamically inhibiting the conversion. In the subsequent stage, the morphological evolution was dominated by the material coarsening process. The volume of open pores decreased during this stage, possibly due to the densification process accompanied by the coarsening. Additionally, the volume fraction of the internal pores increased slightly, indicating that a small amount of the open pores may be enclosed by the surrounding material, transforming into internal pores. After 83 min of isothermal heating at 900 °C in the first cycle, both internal and open pores were still observed in the particles.

At 800 °C, the volume fraction of the open pores decreased, while that of the internal pores increased slightly. CoO near the open pores readily reacted with O₂, promoting its re-oxidation to Co₃O₄. As the density at room temperature of CoO (6.44 g cm⁻³ [35]) is larger than that of Co₃O₄ (6.11 g cm⁻³ [36]), the oxidation process caused the particle volume to increase, reducing the volume of open pores, consistent with our findings here. Literature has described this CoO reoxidation process involves displacement reaction and ambipolar diffusion of Co ions and electrons[37,38]. For the internal pores, it has been confirmed with TEM that there is no pore formation from reoxidation of CoO back to Co₃O₄[39], and thus the increased volume of internal pores at 800 °C was likely due to the enclosure of open pores from the coarsening process.
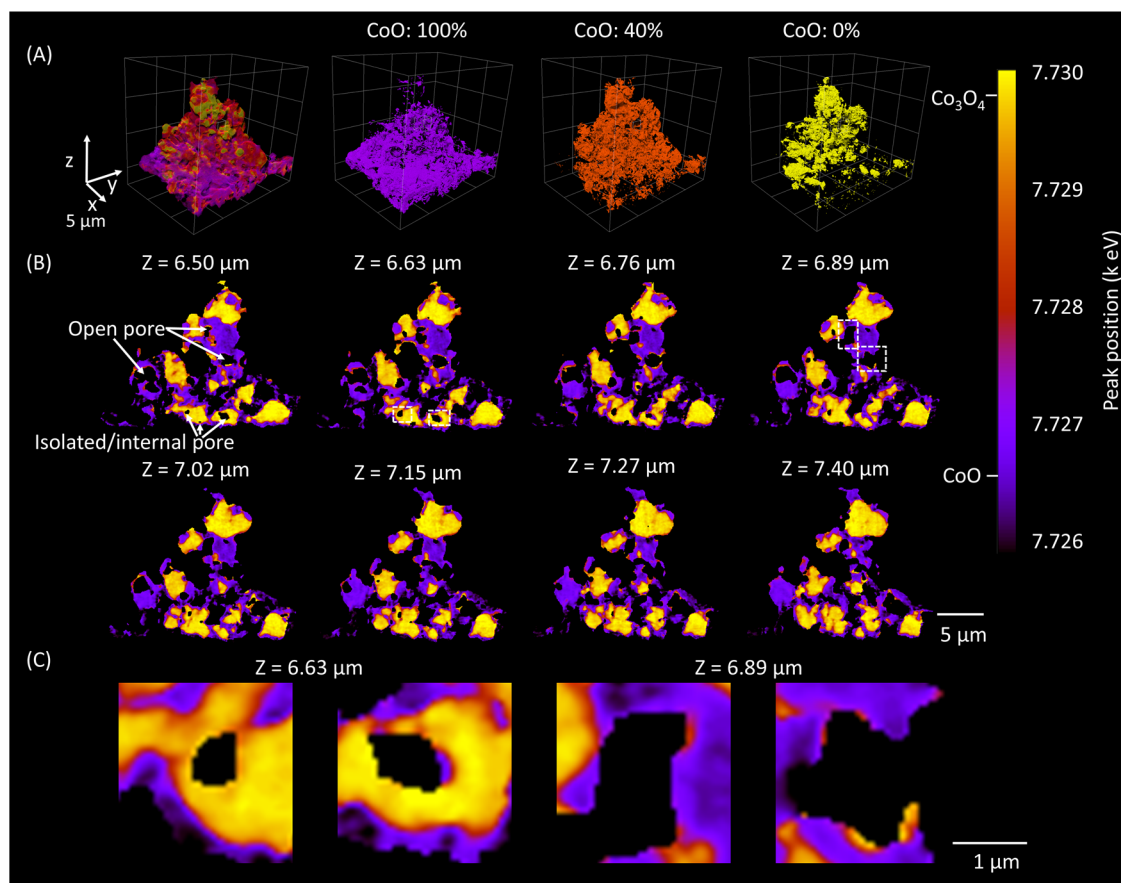
Fig. 7 | 3D XANES analysis of Co$_3$O$_4$ microparticles quenched after the second reduction cycle at 900 °C for 30 min, preserving the high-temperature phases. (**A**) 3D volume rendering based on peak position fitting, showing lower peak position values (corresponding to the CoO phase) predominantly at the particle surface, while higher values (Co$_3$O$_4$ phase) remain in the interior; (**B**) Representative image slices in XY view from the 3D XANES data, illustrating the spatial distribution of CoO and Co$_3$O$_4$ phases, as well as the presence of internal/isolated and open pores, $Z = 0$ is defined as the bottom of the sample in z direction in (**A**); (**C**) The enlarged view in the white dash rectangle in the X-Y views in (**B**) at $Z = 6.63$ and 6.89 μm.

During the second thermal cycle, when heating to 900 °C again, the internal pores formed during the previous re-oxidation process remained within the material. Although many open pores were generated, these internal pores likely inhibited the conversion of Co$_3$O$_4$ to CoO by trapping O$_2$ within them. As discussed in Section 2.2, a large number of internal pores (8.2% volume fraction) were generated within the particles due to coarsening and sintering at 850 °C. Although the internal and isolated pore volume decreased to 7.2% at 800 °C, the trapped O$_2$ created a localized high-concentration environment within these pores, which could inhibit the reduction reaction (Co$_3$O$_4$ to CoO) during the second cycle, as discussed previously for Figs. 2, 3.

To understand the mass transport from high-curvature regions (sharp features with higher chemical potential) to low-curvature regions (smoother features with lower chemical potential) driven by surface energy minimization, the curvature distribution on the particle surface was analyzed. Figure 6 shows the 3D visualization of the mean curvature of the particle during the thermal cycles, along with the corresponding interfacial shape distribution and Gaussian curvature analysis.

As shown in Fig. 6B, regions of the Co$_3$O$_4$ particle with mean curvature near zero (blue areas) generally correspond to relatively smooth surfaces, although they can still include points with either positive or negative Gaussian curvature, reflecting different local geometries. As the temperature increased to 900 °C, high-curvature features developed, leading to noticeable morphological changes. During the isothermal hold at 900 °C, surface coarsening led to a reduction in these sharp features, resulting in smoother morphologies.

The scaled interfacial shape distribution in Fig. 6C clearly shows that point (d) has a greater proportion of low curvature features compared to point (c), indicating a smoother interface. A similar smoothing trend was observed during the second cycle at 900 °C, comparing (g) and (h), the distributions of the principal curvatures (K_1, K_2) shift toward lower values, indicating a smoother surface. A map of the different regions along with their corresponding interfacial shapes has been illustrated in the literature[32]. Features within the particle characterized by $K_1 < 0$ and $K_2 > 0$ exhibit saddle-like curvature[32].

To further quantify these changes, histograms of the mean curvature (H = ($K_1 + K_2$)/2) and Gaussian curvature (H = $K_1 \cdot K_2$) for points (c), (d), (g), and (h) are shown in Fig. 6D. In both cycles, the coarsening process promoted the mass transport from high-curvature regions, associated with sharp features and higher chemical potential, toward lower-curvature regions with smoother geometries and lower chemical potential. As a result, both the mean curvature and Gaussian curvature values for points (d) and (h) shifted closer to zero, indicating the development of more planar surface features[40].

To investigate the spatial distribution of CoO and Co$_3$O$_4$ phases, as well as the presence of internal/isolated and open pores at 900 °C, Co$_3$O$_4$ microparticles were quenched after the second reduction cycle at 900 °C for 30 min to preserve the high-temperature phases. A 3D XANES analysis was then conducted at room temperature, with the results shown in Fig. 7.

In Fig. 7A, the color in the 3D volume rendering represents the peak position of the XANES spectra at the Co K-edge. A peak position of ~7.726 keV corresponds to a region fully converted to the CoO
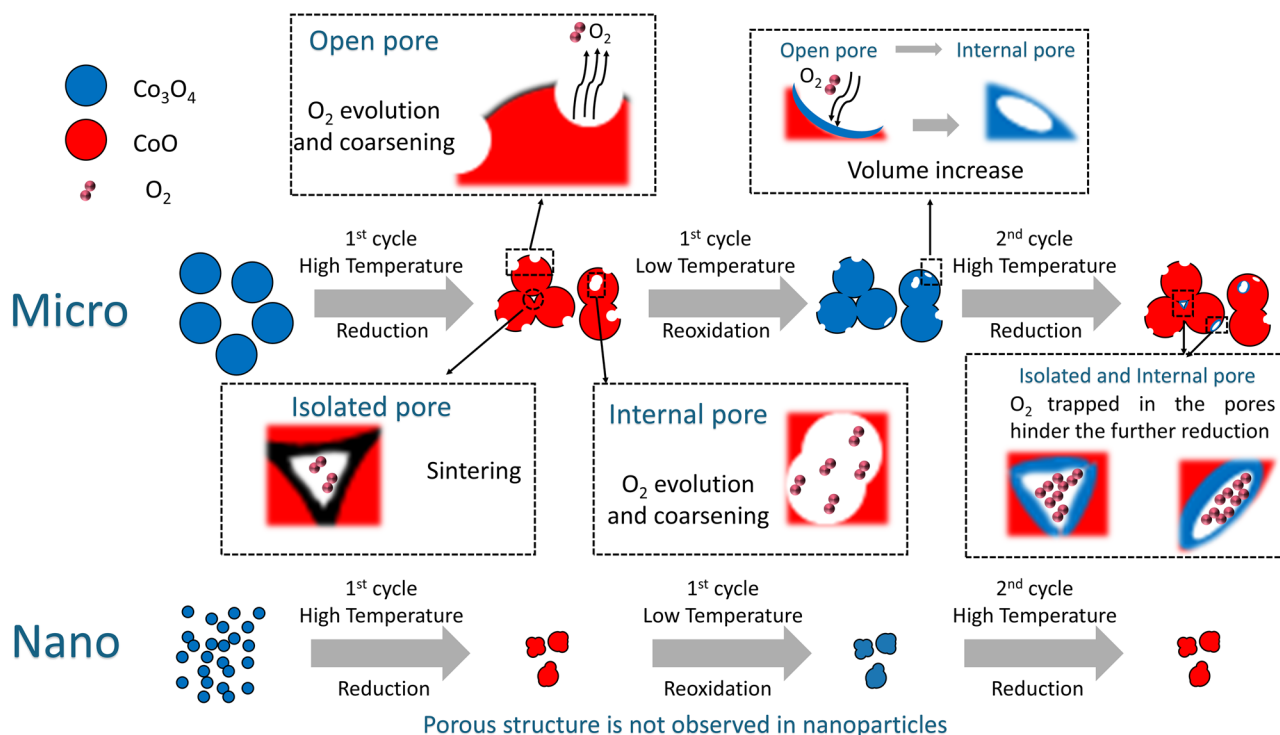
Fig. 8 | Schematic illustration of the mechanism of porous structure formation in Co_3O_4 microparticles and the role of internal and isolated pores in the subsequent reduction process, in contrast to the absence of an apparent porous structure in Co_3O_4 nanoparticles.

phase, while a position of ~7.730 keV corresponds to unconverted Co_3O_4. Since the high-temperature phases were preserved during quenching, the surface regions indicate full conversion to CoO due to the easy release of O_2. In contrast, the interior regions, containing internal and isolated pores that trap O_2 and increase the local O_2 partial pressure, remain largely unconverted as Co_3O_4. The subfigure highlights regions with approximately 40% CoO (mole fraction). In the innermost region, the material remains entirely as unconverted Co_3O_4.

To further illustrate the spatial distribution of CoO and Co_3O_4 phases, as well as the presence of isolated and open pores, representative slices in XY view are shown in Fig. 7B. The enlarged view in the white dashed rectangle in the subfigures ($Z = 6.63$ and $6.89\,\mu m$) is shown in Fig. 7C. Regions near open pores appear purple, indicating the presence of CoO, while areas adjacent to isolated pores appear red or yellow, indicating the retained Co_3O_4. Therefore, the open and internal/isolated pore structures play a critical role in the conversion process: while open pores facilitate gas exchange and promote the reduction reaction, isolated and internal pores likely inhibit the conversion of Co_3O_4 to CoO by trapping evolved O_2, increasing the local oxygen concentration and thereby suppressing further reduction of Co_3O_4.

To summarize the mechanism of porous structure formation in the Co_3O_4 microparticle sample and the influence of internal and isolated pores on the subsequent reduction process, a schematic illustration is shown in Fig. 8.

In summary, when Co_3O_4 microparticles are heated to high temperatures, multiple types of pores are generated. Open and internal pores form because of O_2 evolution, followed by vacancy diffusion and subsequent coarsening. Isolated pores develop between particles due to sintering. Upon cooling to lower temperatures, some open pores may transform into closed pores due to the volume expansion associated with the re-oxidation of CoO to Co_3O_4. During subsequent heating, these closed and internal pores inhibit the reduction of Co_3O_4 to CoO by trapping the evolved O_2, which increases the local oxygen concentration and thereby suppresses further reduction. In contrast, this porous structure is not observed in the Co_3O_4 nanoparticle samples.

The commonly accepted benefit of a porous structure lies in the formation of open pores, which facilitate oxygen release to the surrounding atmosphere. In our study, the volume of open pores is significantly higher than that of internal pores. However, the impact of internal and isolated pores should not be overlooked, as their ability to trap evolved O_2 gases can undermine redox performance. In addition to their role in trapping oxygen, internal and isolated pores can also negatively decrease the thermal conductivity of the material. This reduction in thermal conductivity can hinder efficient heat transfer within the particle, potentially slowing the temperature rise required to drive the endothermic reduction of Co_3O_4. A number of studies have demonstrated this inverse relationship between porosity and thermal conductivity[41–43]. However, in the present study, the sample consists of a thin particle layer attached to the inner wall of a quartz capillary and is heated via radiative transfer from an external furnace. Due to the small sample volume and the predominance of radiative over conductive heating in this configuration, we believe the impact of isolated pores on thermal conduction is negligible in our case.

Post-TXM experiment analysis with SEM for particle sintering

To validate the morphological changes observed via X-ray nanotomography, Co_3O_4 microparticles were subsequently characterized using SEM. For SEM imaging, the microparticles were examined at room temperature directly on the quartz capillaries used for the X-ray experiments, as shown in Fig. 9A, B. Initially, the microparticles were imaged before thermal cycling. As shown in Fig. 9C, the uncycled microparticles exhibited flat, sharply faceted surfaces. In contrast, after one thermal redox cycle (heating to 900 °C, cooling to 800 °C, and then returning to ambient temperature), the particle surfaces became considerably smoother and less faceted, as shown in Fig. 9D. This change in surface morphology resulted from a surface smoothing and coarsening effect during the high-temperature thermal redox cycle, driven by the minimization of total surface energy, as also discussed in the X-ray imaging analysis (Fig. 5)[44]. Notable particle sintering[11,12] was also observed after one cycle, with the apparent
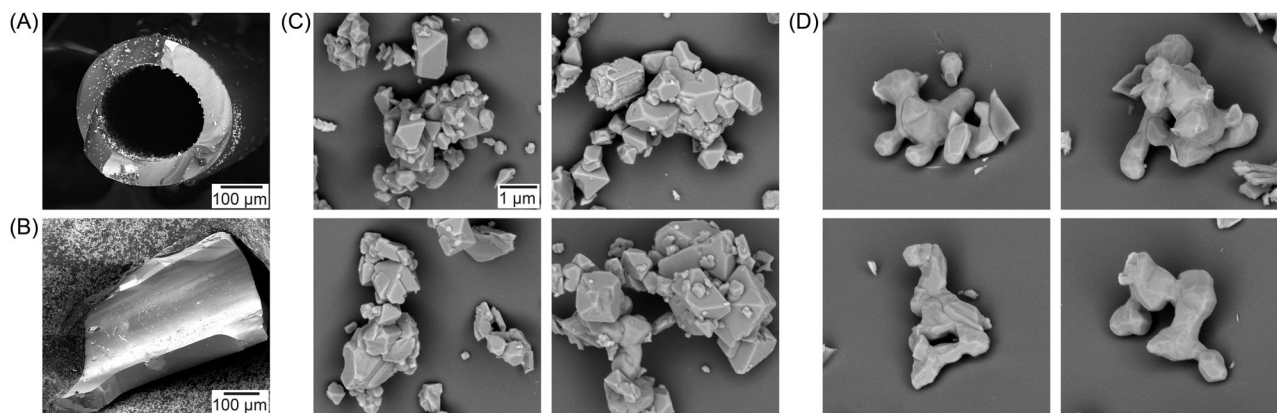
Fig. 9 | Ex situ SEM characterization of morphological changes in Co$_3$O$_4$ microparticles before and after thermal redox cycling during the synchrotron TXM experiment. A Low-magnification SEM image of the open end of a quartz capillary used in the synchrotron TXM experiment, showing Co$_3$O$_4$ microparticles adhering to the inner walls. **B** Broken capillary piece with microparticles on the exposed face, prepared for higher magnification imaging shown in (**C**) and (**D**). Room-temperature SEM images showing morphological changes of microparticles (**C**) before and (**D**) after one thermal redox cycle at the synchrotron TXM experiment (up to 900 °C). The scale bar shown in (**C**) is accurate for all images in (**C**) and (**D**).

merging of small, discrete particle units into larger, continuous microstructures. Both surface coarsening and sintering are likely to contribute to the decrease in specific surface area during thermal redox cycling of Co$_3$O$_4$ as a thermochemical material.

Summary of findings and future perspectives on TCMs

In this study, the 3D morphological and chemical evolution of Co$_3$O$_4$ micro and nanoparticles during thermal cycles in the range of 800 to 900 °C were investigated using thermal analysis, in-situ synchrotron transmission X-ray microscopy, and scanning electron microscopy techniques. The analysis revealed distinct thermal redox behaviors between Co$_3$O$_4$ microparticles and nanoparticles. The TGA analysis indicated that Co$_3$O$_4$ nanoparticles demonstrated faster re-oxidation at 800 °C compared to microparticles. No significant degradation was observed by TGA in either Co$_3$O$_4$ micro or nanoparticles during five thermal redox cycles.

The in-situ chemical mapping by 2D XANES imaging and 3D morphological studies by X-ray nano-tomography confirmed these findings, highlighting the significant differences in the chemical and morphological evolution between the two particle sizes. Nanoparticles exhibited a faster redox conversion rate between Co$_3$O$_4$ and CoO without forming porous structures during the thermal cycles. In contrast, microparticles developed porous structures that potentially hindered the redox conversion. Further investigation of a single microparticle indicated that both open and internal pores formed during the reduction process due to O$_2$ evolution, with the subsequent coarsening primarily driven by surface diffusion. The volume fraction of open pores decreased significantly, while that of the internal pores remained and increased slightly during the re-oxidation process at 800 °C. In subsequent cycles, these internal pores appeared to hinder the reduction process from Co$_3$O$_4$ to CoO by trapping O$_2$, creating a localized high-concentration environment. Internal pores were generated more extensively during cooling from 900 °C and holding at 850 °C due to the back-and-forth conversion between Co$_3$O$_4$ and CoO, which could have a more significant impact on the subsequent reduction process. Post-TXM experiment analysis with SEM revealed that the initial microparticles had flat, sharply faceted surfaces and became smoother and less faceted after the thermal redox cycle due to the coarsening process. Additionally, larger, more continuous microparticle structures were observed due to sintering. These findings demonstrate that Co$_3$O$_4$ serves as a representative model for understanding redox-induced structural evolution in metal oxides, and the mechanistic insights gained here, particularly on pore evolution, sintering, and particle size effects, can be extended to guide future

studies, as well as design and optimization of other thermochemical materials. Moreover, the in situ synchrotron-based imaging methodology used in this work is highly adaptable. It can be applied to a broad range of TCMs under controlled atmospheres or reactive conditions, and with proper containment, even to materials that are corrosive or toxic, thereby providing a versatile platform for investigating chemical and morphological evolution across diverse material systems.

Overall, nanoparticles exhibited a faster and more stable conversion without developing significant porous structures, whereas microparticles were prone to forming internal and isolated pores, which can slow down the reduction process and reduce long-term cycling performance. This highlights the importance of understanding how particle size and pore structure affect degradation during cycling. Future material design should focus on approaches that prevent sintering and coarsening, such as adding dopants to help maintain a stable structure with high surface area. In addition, promoting and preserving open porous networks can improve gas exchange while reducing the formation of isolated pores that limit performance. Applying these particles onto a chemically stable, macroporous support may further enhance structural stability and heat transfer by improving gas flow and reducing densification. Finally, adjusting thermal conductivity and oxygen transport properties through material selection or structure changes may offer additional ways to improve redox performance. Together, these insights provide a practical direction for developing thermochemical materials with better durability and efficiency under thermal cycling conditions.

Methods
Experimental procedure of thermal analysis

The Co$_3$O$_4$ microparticles (<10 µm, 99.0%, Sigma-Aldrich) and nanoparticles (<50 nm, 99.5% trace metal basis, Sigma-Aldrich) were used in the experiments. The thermal redox cycles of Co$_3$O$_4$ micro and nano particles were evaluated using a thermogravimetric and differential scanning calorimetry analyzer (TGA, Mettler Toledo TGA/DSC 3 +) at atmospheric pressure. The schematic TGA experimental setup is shown in Fig. 10A. Approximately 3.0 mg of sample was loaded into a 70 µL alumina crucible and thermally cycled between the temperatures of 800 °C, 850 °C and 900 °C. The temperature was initially kept at 800 °C[19] to remove impurities from the particle surface. A ramping rate of 50 °C/min was applied during both the heating and cooling cycles. Throughout the tests, sample mass and temperature were monitored at a sampling rate of 1 datapoint per second.
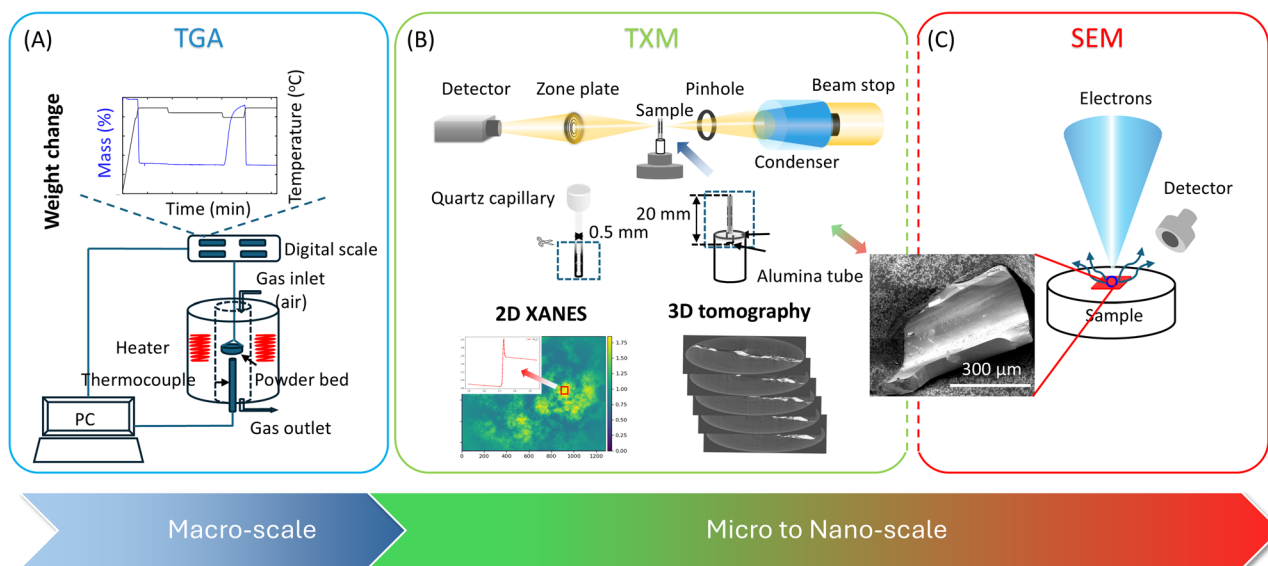
Fig. 10 | Research concept and schematic experimental setup for the kinetics study of Co_3O_4 micro and nano particles in thermal redox cycles. (**A**) TGA setup measuring weight change of samples in macro-scale. **B** In-situ synchrotron TXM setup tracking the chemical and morphological evolution of samples in microns and tens of nm length scale. **C** SEM setup analyzing morphologies for the post-TXM sample.

In-situ synchrotron X-ray nano-tomography and XANES imaging

The schematic of the in-situ synchrotron TXM setup with the capillary sample preparation is shown in Fig. 10B.

The TXM sample preparation of the micro and nanoparticles follows the procedure described below. First, the Co_3O_4 particles were loaded into an open-ended quartz capillary (Charles Supper, 05-QZ) with a 500 µm outer diameter and 10 µm wall thickness. After filling, the particles were poured out, leaving only a thin layer adhered to the inner wall to ensure the collection of a high-quality transmission signal. The funnel end was then removed, resulting in a 20 mm long capillary containing the remaining particles. Afterward, the capillary was attached to an alumina tube (2 mm OD, 1 mm ID, 28 mm length) using an alumina-based ceramic adhesive (Resbond™ 989). In-situ 2D XANES imaging and nano-tomography were conducted on the particle samples enclosed in the capillary, during thermal redox cycles in a temperature range of 800 °C to 900 °C with a versatile, compact heater after proper calibration[45] at the Full Field X-ray Imaging beamline (FXI, 18-ID)[46] at the National Synchrotron Light Source-II (NSLS-II) at Brookhaven National Laboratory (BNL).

The images from the TXM at the FXI beamline were captured using a lens-coupled CCD detector with 2560 × 2160 pixels, providing a field of view of 46.8 µm × 55.48 µm. A camera binning of 2 × 2 was used, resulting in an effective pixel size of 43.34 nm. For nano-tomography, the X-ray incident energy was set to 8.0 keV, which is the designed energy for the objective zone plate. It is also slightly higher than the Co K-edge (7.709 keV), which provides a good contrast between particle and air regions. The nano-tomography was conducted at a fly scan mode, with a rotation speed of 8 °/s to capture the morphological evolution at a higher temporal and spatial resolution to minimize the impact of particle movements on the imaging quality due to the elevated temperature. The exposure time for each projection image was 0.05 s. The full tomography was collected with a 180° rotation capturing about 450 projections, with a total acquisition time of 0.5 to 1.0 min per tomographic scan. For the 2D and 3D XANES imaging, scans were conducted at X-ray energy across the Co K-edge, from 7500–7709 eV in 100 eV steps, 7710–7715 eV in 5 eV steps, 7715–7735 eV in 1 eV steps, and 7740–8000 eV in 100 eV steps. With fewer energy points, each 2D XANES imaging scan took about 4.5 min to ensure that the chemical evolution was well captured. The 3D XANES scan was carried out on microparticle samples quenched to room temperature after the second reduction cycle at 900 °C for 30 min, in order to preserve the high-temperature phases. 3D XANES was measured by collecting tomography as a function of energy, following the same energy points mentioned above. The tomography at different energies was reconstructed and subsequently registered to ensure proper alignment, enabling accurate XANES fitting.

3D volumes were reconstructed from tomography projection images using gridrec algorithm implemented in Tomopy[47] package. Post image processing of the 3D tomographic reconstruction stack images, including data at different energies and different time points, was conducted using the Crop3D and Median (3D) plugin in the FIJI package of ImageJ[48], as well as Python packages including Skimage[49], Numpy[50] and Scipy[51] to perform cropping, filtering, segmentation and volume registration. Volume registration from fast Fourier transforms of the 3D volumes was used to align the whole tomography. Thresholding segmentation was performed to differentiate the solid phase (Co_3O_4 and CoO mixture) and air. Watershed image segmentation and flood fill method was used to identify a single particle and the internal pores. The open pores of the particle were identified with further image processing, and the details are shown in Fig. S7. The image profiles of mean curvature and Gaussian curvature were calculated using Tomviz (version 1.10), an open-source software package[52]. The principal curvatures were then derived from the mean curvature and the Gaussian curvature. The interfacial shape distribution (ISD) plot was then generated based on the curvature values using customized code developed in our previous study[40]. The processed image stacks were then visualized in 2D using ImageJ and in 3D using Dragonfly software (version 2020.1, Comet Technologies Canada Inc.)[53]. The volume and surface area of the particles were calculated using Dragonfly software after proper segmentation. The XANES data were processed using PyXAS[27,54] and Athena software[55].

Standard X-ray absorption spectra of CoO and Co_3O_4 were collected at the Inner Shell Spectroscopy beamline (ISS, 8-ID) at NSLS-II at BNL (Fig. S8). The white line position of CoO is 7726.4 eV, while that of Co_3O_4 is 7729.8 eV. Therefore, in the 2D XANES imaging and the 3D XANES image stacks data, the fitted white line position at each pixel can be representative of the reduction (CoO) and oxidation (Co_3O_4) phases in the particles. Here, the spectrum at each pixel is a linear combination of CoO and Co_3O_4 spectra proportional to the amount of Co in each phase, from the projected views. The fitted white line

positions between 7726.4 and 7729.8 eV do not indicate an intermediate oxidation state, but rather the ratio of these two phases. The corresponding fitted white line positions of the combined spectra of Co_3O_4 and CoO are shown in Fig. S9. Thus, the fraction of Co in the CoO phase in each pixel can be calculated based on the white line position. Using the amount of Co estimated from the X-ray absorption, the conversion depending on the amount of Co can also be calculated. The detailed calculation method is shown in Fig. S10.

SEM sample preparation and characterization

The post-TXM Co_3O_4 microparticles were characterized with SEM using two methods. With the first method, microparticles were imaged directly through the open end of the microcapillary using a low-energy backscattered electron detector on a TESCAN Solaris Ga-FIB-SEM operated at 2 kV accelerating voltage with a 300 pA beam current in UH-Resolution mode. Second, the microcapillary was broken, and a piece was mounted on a standard SEM stub using Ag paint and subsequently sputter-coated with 5 nm Au. The broken microcapillary piece is shown in Fig. 10C. Secondary electron images were then acquired on a FEI Nova NanoSEM 630 operated at 5 kV accelerating voltage with a 3.6 nA beam current.

Data availability

The digital data for all figures, tables, charts, and any other media contained in this publication and its associated supporting information files are available on the Zenodo repository, under Digital Object Identifier (DOI): 10.5281/zenodo.17211114. Source data are provided with this paper.

Code availability

The custom code used for data processing and analysis is available on the GitHub repository, under Digital Object Identifier (DOI): https://github.com/SBU-Chen-Wiegart/Co3O4.

References

1. Pardo, P. et al. A review on high temperature thermochemical heat energy storage. *Renew. Sustain. Energy Rev.* **32**, 591–610 (2014).
2. Gil, A. et al. State of the art on high-temperature thermal energy storage for power generation. Part 1—Concepts, materials and modellization. *Renew. Sustain. energy Rev.* **14**, 31–55 (2010).
3. Tescari, S. et al. Numerical model to design a thermochemical storage system for a solar power plant. *Energy Procedia* **75**, 2137–2143 (2015).
4. Singh, A. et al. Solar thermochemical heat storage via the Co_3O_4/CoO looping cycle: storage reactor modelling and experimental validation. *Sol. Energy* **144**, 453–465 (2017).
5. Block, T. & Schmücker, M. Metal oxides for thermochemical energy storage: a comparison of several metal oxide systems. *Sol. Energy* **126**, 195–207 (2016).
6. Neises, M. et al. Solar-heated rotary kiln for thermochemical energy storage. *Sol. Energy* **86**, 3040–3048 (2012).
7. Liu, J., Baeyens, J., Deng, Y., Wang, X. & Zhang, H. High temperature Mn_2O_3/Mn_3O_4 and Co_3O_4/CoO systems for thermo-chemical energy storage. *J. Environ. Manag.* **267**, 110582 (2020).
8. Silakhori, M., Jafarian, M., Arjomandi, M. & Nathan, G. J. Thermogravimetric analysis of Cu, Mn, Co, and Pb oxides for thermochemical energy storage. *J. Energy storage* **23**, 138–147 (2019).
9. Wong, B. Thermochemical heat storage for concentrated solar power. *Final Report for the US Department of Energy*. (2011).
10. Hutchings, K. N., Wilson, M., Larsen, P. A. & Cutler, R. A. Kinetic and thermodynamic considerations for oxygen absorption/desorption using cobalt oxide. *Solid State Ion.* **177**, 45–51 (2006).
11. Nekokar, N., Pourabdoli, M., Hamidi, A. G. & Uner, D. Effect of mechanical activation on thermal energy storage properties of Co_3O_4/CoO system. *Adv. Powder Technol.* **29**, 333–340 (2018).
12. Block, T., Knoblauch, N. & Schmücker, M. The cobalt-oxide/iron-oxide binary system for use as a high-temperature thermochemical energy storage material. *Thermochim. Acta* **577**, 25–32 (2014).
13. Agrafiotis, C., Roeb, M., Schmücker, M. & Sattler, C. Exploitation of thermochemical cycles based on solid oxide redox systems for thermochemical storage of solar heat. Part 1: testing of cobalt oxide-based powders. *Sol. Energy* **102**, 189–211 (2014).
14. Liu, L. et al. Superior thermochemical energy storage performance of the Co_3O_4/CoO redox couple with a cubic micro-nanostructure. *J. Energy Storage* **43**, 103167 (2021).
15. Pagkoura, C. et al. Cobalt oxide-based structured bodies as redox thermochemical heat storage medium for future CSP plants. *Sol. Energy* **108**, 146–163 (2014).
16. Agrafiotis, C., Tescari, S., Roeb, M., Schmücker, M. & Sattler, C. Exploitation of thermochemical cycles based on solid oxide redox systems for thermochemical storage of solar heat. Part 3: cobalt oxide monolithic porous structures as integrated thermochemical reactors/heat exchangers. *Sol. Energy* **114**, 459–475 (2015).
17. Carrillo, A. J., Serrano, D. P., Pizarro, P. & Coronado, J. M. Thermochemical heat storage based on the Mn_2O_3/Mn_3O_4 redox couple: influence of the initial particle size on the morphological evolution and cyclability. *J. Mater. Chem. A* **2**, 19435–19443 (2014).
18. Han, X. et al. Al-and Cr-doped Co_3O_4/CoO redox materials for thermochemical energy storage in concentrated solar power plants. *Sol. Energy Mater. Sol. Cells* **260**, 112475 (2023).
19. Agrafiotis, C., Roeb, M. & Sattler, C. Hybrid sensible/thermochemical solar energy storage concepts based on porous ceramic structures and redox pair oxides chemistry. *Energy Procedia* **69**, 706–715 (2015).
20. Liu, L. et al. Lattice matching strategy in Cu-based oxides for large-scale and long-term thermochemical energy storage. *Energy Storage Mater.* **73**, 103825 (2024).
21. Sun, J. et al. Evaluation of thermochemical energy storage performance of Fe-/Mn-doped, Zr-stabilized, CaO-based composites under different thermal energy storage modes. *ACS Appl. Energy Mater.* **5**, 4903–4915 (2022).
22. Sinha, P. et al. Surface area determination of porous materials using the Brunauer–Emmett–Teller (BET) method: limitations and improvements. *J. Phys. Chem. C* **123**, 20195–20209 (2019).
23. Kankanallu, V. R. et al. Elucidating a dissolution–deposition reaction mechanism by multimodal synchrotron X-ray characterization in aqueous Zn/MnO_2 batteries. *Energy Environ. Sci.* **16**, 2464–2482 (2023).
24. Bak, S.-M., Shadike, Z., Lin, R., Yu, X. & Yang, X.-Q. In situ/operando synchrotron-based X-ray techniques for lithium-ion battery research. *NPG Asia Mater.* **10**, 563–580 (2018).
25. Liu, X. et al. Heterogeneous 3D morphological evolution of ni microparticles in molten salts: visualized by operando synchrotron x-ray nano-tomography. *JOM* **75**, 1006–1018 (2023).
26. Liu, X. et al. Formation of three-dimensional bicontinuous structures via molten salt dealloying studied in real-time by in situ synchrotron X-ray nano-tomography. *Nat. Commun.* **12**, 3441 (2021).
27. Ge, M. & Lee, W.-K. PyXAS–an open-source package for 2D X-ray near-edge spectroscopy analysis. *J. Synchrotron Radiat.* **27**, 567–575 (2020).
28. Pattammattel, A. et al. High-sensitivity nanoscale chemical imaging with hard X-ray nano-XANES. *Sci. Adv.* **6**, eabb3615 (2020).
29. Brinkmanf, J. Mechanism of pore formation associated with the Kirkendall effect. *Acta Metall.* **3**, 140–145 (1955).
30. Sieradzki, K. Curvature effects in alloy dissolution. *J. Electrochem. Soc.* **140**, 2868 (1993).
31. Kwon, Y., Thornton, K. & Voorhees, P. The topology and morphology of bicontinuous interfaces during coarsening. *Europhys. Lett.* **86**, 46005 (2009).

32. Kammer, D. & Voorhees, P. The morphological evolution of dendritic microstructures during coarsening. *Acta Mater.* **54**, 1549–1558 (2006).

33. Herring, C. Effect of change of scale on sintering phenomena. *J. Appl. Phys.* **21**, 301–303 (1950).

34. Liu, X. et al. Environmentally friendly Zr-based conversion nanocoatings for corrosion inhibition of metal surfaces evaluated by multimodal X-ray analysis. *ACS Appl. Nano Mater.* **2**, 1920–1929 (2019).

35. Nam, K. M. et al. Syntheses and characterization of wurtzite CoO, rocksalt CoO, and spinel Co_3O_4 nanocrystals: their interconversion and tuning of phase and morphology. *Chem. Mater.* **22**, 4446–4454 (2010).

36. Mariano, A., Pastoriza-Gallego, M. J., Lugo, L., Mussari, L. & Piñeiro, M. M. Co_3O_4 ethylene glycol-based nanofluids: thermal conductivity, viscosity and high pressure density. *Int. J. Heat. Mass Transf.* **85**, 54–60 (2015).

37. Przybylski, K. & Smeltzer, W. High temperature oxidation mechanism of CoO to Co_3O_4. *J. Electrochem. Soc.* **128**, 897 (1981).

38. Żyła, M. et al. The formation of the Co_3O_4 cobalt oxide within the CoO substrate. *Corros. Sci.* **112**, 536–541 (2016).

39. Ha, D.-H., Moreau, L. M., Honrao, S., Hennig, R. G. & Robinson, R. D. The oxidation of cobalt nanoparticles into Kirkendall-hollowed CoO and Co_3O_4: The diffusion mechanisms and atomic structural transformations. *J. Phys. Chem. C.* **117**, 14303–14312 (2013).

40. Lin, Y.-C. et al. Unveiling 3D morphology of multiscale micro-nanosilver sintering for advanced electronics manufacturing by ptychographic x-ray nanotomography. *Adv. Eng. Mater.* **22**, 1901250 (2020).

41. Resl, O., Chabičovský, M., Hnízdil, M., Kotrbáček, P. & Raudenský, M. in *Proceedings of the 9th International Conference of Fluid Flow, Heat and Mass Transfer (FFHMT'22)*, **125**, (2022).

42. Sumirat, I., Ando, Y. & Shimamura, S. Theoretical consideration of the effect of porosity on thermal conductivity of porous materials. *J. Porous Mater.* **13**, 439–443 (2006).

43. Chen, L. et al. Giant reduction in thermal conductivity of Co_3O_4 with ordered mesopore structures. *Microporous Mesoporous Mater.* **296**, 109969 (2020).

44. Liu, X. et al. Temperature-dependent morphological evolution during corrosion of the Ni-20Cr alloy in molten salt revealed by multiscale imaging. *ACS Appl. Mater. Interfaces* **15**, 13772–13782 (2023).

45. Antonelli, S. et al. Versatile compact heater design for in situ nanotomography by transmission X-ray microscopy. *Synchrotron Radiat.* **27**, 746–752 (2020).

46. Ge, M. One-minute nano-tomography using hard X-ray full-field transmission microscope. Appl. Phys. Lett. **113**, 083109 (2018).

47. Gürsoy, D., De Carlo, F., Xiao, X. & Jacobsen, C. TomoPy: a framework for the analysis of synchrotron tomographic data. *Synchrotron Radiat.* **21**, 1188–1193 (2014).

48. Arganda-Carreras, I. et al. Trainable Weka Segmentation: a machine learning tool for microscopy pixel classification. *Bioinformatics* **33**, 2424–2426 (2017).

49. Van der Walt, S. et al. scikit-image: image processing in Python. *PeerJ* **2**, e453 (2014).

50. Harris, C. R. et al. Array programming with NumPy. *Nature* **585**, 357–362 (2020).

51. Jones, E., Oliphant, T. & Peterson, P. & others. *SciPy: open source scientific tools for Python.* http://www.scipy.org/ (2001).

52. Schwartz, J. et al. Real-time 3D analysis during electron tomography using tomviz. *Nat. Commun.* **13**, 4458 (2022).

53. Comet Technologies Canada Inc., Montreal, Canada. Dragonfly 2020.1 [Computer software], https://dragonfly.comet.tech/ (2022).

54. Li, Z. et al. Highly sensitive 2D X-ray absorption spectroscopy via physics-informed machine learning. *npj Comput. Mater.* **10**, 128 (2024).

55. Ravel, B. & Newville, M. ATHENA, ARTEMIS, HEPHAESTUS: data analysis for X-ray absorption spectroscopy using IFEFFIT. *J. synchrotron Radiat.* **12**, 537–541 (2005).

Acknowledgments

Author contributions

Y.P. and Y.-c.K.C. conceived the project and designed the study. Y.P. carried out the main investigation, including the synchrotron TXM experiments and data analysis, and drafted the manuscript. L.Z. performed TGA experiments and analysis under the supervision of S.C. Y.Z. conducted DSC measurements and analysis. M.G. and X.X. aligned and set up the TXM beamline and supported the experiments. C.-c.C. participated in part of the TXM experiments and contributed to TXM data analysis. M.V.W. and J.M. conducted SEM characterization. K.J. and J.V. provided conceptual input and supervision. Y.-c.K.C. supervised the overall research, contributed to data interpretation, and co-wrote and edited the manuscript. All authors contributed to the discussion of the results and the editing of the manuscript.

Competing interests

The authors declare no competing interests.

Additional information